Astronomy & Astrophysics manuscript no. aa
November 10, 2019

The tilt of the velocity ellipsoid in the Milky Way with *Gaia* DR2

Jorrit H. J. Hagen[1], Amina Helmi[1], P. Tim de Zeeuw[2,3], and Lorenzo Posti[1]

[1] Kapteyn Astronomical Institute, University of Groningen, Landleven 12, 9747 AD Groningen, The Netherlands
e-mail: hagen@astro.rug.nl
[2] Sterrewacht Leiden, Leiden University, Postbus 9513, 2300 RA Leiden, The Netherlands
[3] Max Planck Institute for Extraterrestrial Physics, Giessenbachstrasse 1, 85748 Garching, Germany

Received 13 February 2019 / Accepted XX Month 2019

ABSTRACT

The velocity distribution of stars is a sensitive probe of the gravitational potential of the Galaxy, and hence of its dark matter distribution. In particular, the shape of the dark halo (e.g. spherical, oblate, prolate) determines velocity correlations, and different halo geometries are expected to result in measurable differences. We here explore and interpret the correlations in the (v_R, v_z)-velocity distribution as a function of position in the Milky Way. We select a high quality sample of stars from the *Gaia* DR2 catalog, and characterise the orientation of the velocity distribution or tilt angle, over a radial distance range of $[3-13]$ kpc and up to 4 kpc away from the Galactic plane while taking into account the effects of the measurement errors. The velocity ellipsoid is consistent with spherical alignment at $R \sim 4$ kpc, while it progressively becomes shallower at larger Galactocentric distances and is cylindrically aligned at $R = 12$ kpc for all heights probed. Although the systematic parallax errors present in *Gaia* DR2 likely impact our estimates of the tilt angle at large Galactocentric radii, possibly making it less spherically aligned, their amplitude is not enough to explain the deviations from spherical alignment. We find that the tilt angles do not strongly vary with Galactic azimuth and that different stellar populations depict similar tilt angles. We introduce a simple analytic function that describes well these trends over the full radial range explored.

Key words. Galaxy: kinematics and dynamics, Galaxy: disk

1. Introduction

The second data release of the *Gaia* space mission (Gaia Collaboration et al. 2018a) contains more than 1.3 billion stars with measured proper motions and positions and a subset of over 7 million stars with full six-dimensional (6-d) phase-space information. The availability of the motions and positions of stars in the Milky Way and its satellite galaxies has already led to new insights on the Galaxy (e.g. Antoja et al. 2018; Poggio et al. 2018; Helmi et al. 2018; Price-Whelan & Bonaca 2018), and many more discoveries will likely follow before *Gaia*'s next data release.

Studies of the Galaxy provide insight into the formation and evolution of galaxies in general, and hence on elements of the cosmological paradigm. For example, detailed dynamical modelling of the Milky Way and its satellites, and in particular of their mass distribution provide critical constraints on the nature of dark matter (e.g. Bonaca et al. 2018). Mass models of the Galaxy such as those by e.g. McMillan (2011); Piffl et al. (2014); McMillan (2017) have been developed to fit many different observational constraints simultaneously, although this is very challenging. Many works therefore often focus on a specific aspect such as, for example, the characterisation of the velocity distribution across the Galaxy.

The in-plane velocity distribution $f(v_R, v_\phi)$ in the Solar vicinity has long been known to be complex, with many moving groups known to exist (e.g. Proctor 1869; Eggen 1965; Dehnen 1998; Antoja et al. 2008). With *Gaia* DR2 the level of detail visible in the velocity distribution of stars has increased immensely (see e.g. Gaia Collaboration et al. 2018b; Antoja et al. 2018), and a plethora of substructures have become apparent. On the other hand, the two-dimensional velocity distribution including the radial and vertical velocity components $f(v_R, v_z)$ shows significantly less substructure and the traditional velocity moments can still, to first order, describe the data well.

Such velocity moments and thus the axial ratios of the velocity ellipsoid, however, depend on the stellar distribution function and will be different for different populations of stars. In contrast, its orientation (or better known as alignment or tilt) is directly related to (the shape of) the underlying gravitational potential in which the stars move (e.g. van de Ven et al. 2003; Binney & Tremaine 2008; Binney & McMillan 2011; An & Evans 2016) and will be the focus of this paper.

Nearly spherically aligned velocity ellipsoids have been found for the halo (Smith et al. 2009; Bond et al. 2010; King et al. 2015; Evans et al. 2016) by mainly using data from the Sloan Digital Sky Survey (York et al. 2000). Similar findings were obtained by Posti et al. (2018) for dynamically selected nearby halo stars. These authors obtained full 6-d phase-space information by combining radial velocity measurements from the Radial Velocity Experiment (RAVE DR5, Kunder et al. 2017) to the 5-d subset of the *Gaia* DR1 catalog (Gaia Collaboration et al. 2016a). Most recently, Wegg et al. (2018) used 15651 RR Lyrae halo stars with accurate proper motions from *Gaia* DR2 and also inferred a nearly spherically aligned velocity ellipsoid over a large range of distances between 1.5 and 20 kpc from the Galactic centre. When fed into the Jeans equations, this result seems to imply a spherical dark matter distribution.

Studies focusing on the orientation of the velocity ellipsoid in local samples of the Milky Way disk have also been consistently reporting (close to) spherical alignment. Siebert et al. (2008) have used RAVE DR2 and found a tilt angle γ equal to $7.3^\circ \pm 1.8^\circ$ for red clump stars at $R = R_\odot$ and $z = 1$ kpc, where $\gamma_{\rm sph} = 7.1^\circ$ would be expected for spherical alignment at this

location. Casetti-Dinescu et al. (2011) found 8.6° ± 1.8° for a sample of stars with heights between 0.7 and 2.0 kpc and representative of the metal-rich thick disk, which can be compared to the expected $\gamma_{\rm sph} = 8.0°$ given the mean location of the sample. Subsequently, Smith et al. (2012) reinforced these findings using data from the Sloan Digital Sky Survey DR7 (SDSS, Abazajian et al. 2009). Binney et al. (2014) using RAVE data, and Büdenbender et al. (2015), using Sloan Extension for Galactic Understanding and Exploration (SEGUE, Yanny et al. 2009), characterised the tilt angle around the Galactic radius of the Sun up to $z \sim 2.0$ kpc by $\gamma(z) \approx a_0 \arctan(z/R_\odot)$. They found $a_0 \sim 0.8$ and $a_0 = 0.9 \pm 0.04$ respectively, values close to, but significantly different from, spherical alignment for which $a_0 = 1.0$. Recently, Mackereth et al. (2019) have analysed the kinematics of mono-age, mono-[Fe/H] populations for both low and high [α/Fe] samples. They have cross matched the Apache Point Observatory Galactic Evolution Experiment (APOGEE DR14, Majewski et al. 2017) with Gaia DR2 to obtain a sample of 65,719 red giant stars located between 4 kpc and 13 kpc in Galactic radius and up to 2 kpc from the Galactic plane. Mackereth et al. (2019) report that the tilt angles found are consistent with spherical alignment for all populations, although they note that the uncertainties are very large.

In this work we characterise the orientation of the velocity ellipsoid over a larger section of the Milky Way by using an accurate dataset of more than 8 million stars from *Gaia* DR2. The paper is organised as follows. In Sect. 2 the dataset is introduced as well as the selection criteria applied. In Sect. 3 we characterise the velocity distribution and the measurement errors. The results are presented in Sect. 4. In that section we also explore differences with azimuth, investigate trends with stellar populations, and put forward a fit that reproduces the variation of the tilt angle with position in the Galaxy. In Sect. 5 we explore the effect of systematic errors on our measurements, and discuss our findings in the context of Galactic models, including those with separable potentials. We summarise in Sect. 6.

2. Data

We use the subset of *Gaia* DR2 with full 6-d information (Gaia Collaboration et al. 2018b) and construct a high quality sample by selecting those stars with 20% relative parallax errors, i.e. $\varpi/\epsilon(\varpi) > 5$. This allows us to compute the distances as $d = 1/\varpi$, and minimize the possible bias from inverting the parallaxes as a proxy for distances.

Following the recommendation of Gaia Collaboration et al. (2018a), we have not attempted to correct for the reported overall parallax offset of -29μas (Lindegren et al. 2018), nor for its local variations. We therefore limit our sample to distances up to 5 kpc ($\varpi \gtrsim 200\mu$as). The effects of uncertain parallaxes are further discussed in Sect. 5.1.

We extend the sample by including radial velocities from other (spectroscopic) surveys. We have cross matched the full *Gaia* DR2 catalog with the Large Sky Area Multi-Object Fiber Spectroscopic Telescope (LAMOST DR4, Cui et al. 2012), RAVE DR5, and APOGEE DR14. As is the case for the spectroscopic sample delivered as part of *Gaia* DR2 (Arenou et al. 2018), we only consider stars whose radial velocity errors have been estimated to be smaller than 20 km/s. If a star has radial velocity measurements from more than one survey, we take the measurement with the smallest quoted error. By adding radial velocities from these other surveys, while considering the same parallax (error) cuts as for the 6-d sample, this results in an increase of 2,312,605 stars (+37%) leading to a total of 8,512,552 stars with accurate full phase-space information. Stars with $d < 1$ kpc, typically have distances better than 5% (median 1.8%) and for stars at $4 < d < 5$ kpc the relative distance errors are in between 5% and 20% (median 12.8%).

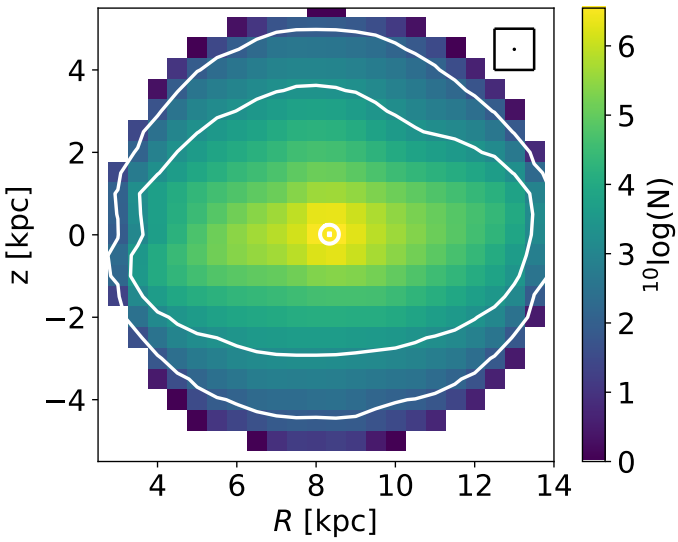

Fig. 1. Star counts from our high quality *Gaia* DR2 6-d sample in bins of width 1.0 kpc in R and z, as indicated by the box in the upper right corner. The central coordinates of the bins are separated by 0.5 kpc in R and z, thus the bins are not fully independent. The white contours indicate the location of bins with 2,000 (inner contour) or 100 (outer contour) stars. The position of the Sun is indicated by the white symbol. Only stars with $\varpi > 0.2$ mas, and $\varpi/\epsilon(\varpi) > 5$ are part of our sample.

Fig. 1 shows the extent of our sample in a number density map. To compute the Galactocentric cylindrical coordinates (R, z, ϕ), we assume $R_\odot = 8.3$ kpc (Schönrich 2012) and $z_\odot = 0.014$ kpc (Binney et al. 1997, and $\phi_\odot = 180°$) for the position of the Sun. Because of the imposed maximum distances to the stars, the sample extends from $R = 3.3$ kpc up to $R = 13.8$ kpc and reaches up to $z = \pm 5$ kpc. The white contours in Fig.1 indicate the location of bins containing 2,000 and 100 stars respectively. This shows that Galactic heights up to ~ 4 kpc are still covered with a statistically significant number of stars.

We derive the velocities of the stars in our sample in a Galactocentric cylindrical coordinate system (v_R, v_z, v_ϕ). For the motion of the Local Standard of Rest (LSR), i.e. the velocity of a circular orbit at $R = R_\odot$ we assume $v_c(R_\odot) = 240$ km/s (Piffl et al. 2014; Reid et al. 2014). The peculiar motion of the Sun with respect to the LSR is taken to be $(U, V, W)_\odot = (11.1, 12.24, 7.25)$ km/s (Schönrich et al. 2010), where U denotes motion radially inward and V in the direction of Galactic rotation (both in the Galactic plane), and W perpendicular to the Galactic plane and in the direction of the Galactic north pole. We propagate the errors and correlations in the observables to determine the errors on the velocities (and their correlations). The median velocity errors for the stars in our sample at $d < 1$ kpc are ~ 1 km/s for the v_R-, v_z-, and v_ϕ-components. At $4 < d < 5$ kpc the median errors are in the range from 2.9 to 5.4 km/s.

The characterisation of the kinematics, in terms of the mean motions and velocity dispersions, of a large part of the Milky Way disk have been presented in Gaia Collaboration et al. (2018b) using the 6-d dataset from *Gaia* DR2. This characterisation has put on firm ground the evidence of the presence of streaming motions in all velocity components (Siebert et al. 2008; Williams et al. 2013; Tian et al. 2017; Carrillo et al. 2018)

and revealed a large amount of substructure in the velocity distributions. Analysis of our extended dataset confirms these findings, and we therefore, in this paper, proceed to focus on the correlation between the radial and vertical velocity components across a large fraction of the Milky Way galaxy.

3. Methods

The 3D velocity distribution of stars $f(v_\phi, v_R, v_z)$ at a given point in the Galaxy may be characterised by its various moments. As described in the Introduction, the tilt of the velocity ellipsoid refers to the orientation of the 2D velocity distribution $f(v_R, v_z)$, which would be obtained by integrating over v_ϕ. As shown in Smith et al. (2009) and Büdenbender et al. (2015), this is equivalent to taking the moments of the 3D velocity distribution and neglecting the cross terms with v_ϕ. These cross-terms are interesting in their own right, as they reveal also other physical mechanisms at work, such as for example the presence of substructures associated to resonances induced by the rotating Galactic bar (Dehnen 1998), but are not the focus of this work.

3.1. The tilt angle: the orientation of the velocity ellipse

In the Galactocentric cylindrical coordinate system we define the tilt angle γ, following e.g. Smith et al. (2009), as:

$$\tan(2\gamma) = \frac{2\mathrm{cov}(v_R, v_z)}{\mathrm{var}(v_R) - \mathrm{var}(v_z)}\,, \tag{1}$$

which therefore takes values from −45 to +45 degrees, and is measured counterclockwise (i.e. from the v_R-axis towards the positive v_z-axis). For exact cylindrical alignment $\gamma_{\rm cyl} = 0°$ and the major and minor axis align with the Galactocentric cylindrical coordinates.

It is also possible to define a tilt angle α with respect to the spherical coordinate system (r, θ, ϕ), where $\tan(\theta) \equiv R/z$, i.e.:

$$\tan(2\alpha) \equiv \frac{2\mathrm{cov}(v_r, v_\theta)}{\mathrm{var}(v_r) - \mathrm{var}(v_\theta)}\,. \tag{2}$$

The tilt angle α thus measures directly the deviation from spherical alignment, which corresponds to $\alpha = 0°$. In such a case one of the principal axes of the ellipse points to the Galactic centre. The relation between α and γ at every (R, z) is

$$\tan(2\gamma) = -\tan(2\theta + 2\alpha). \tag{3}$$

From now on, we always refer to the tilt angle γ, i.e. as defined in the cylindrical coordinate system, unless stated otherwise. To explore the spatial variation of the tilt angle we measure the intrinsic moments of Eq. 1 after projecting all stars onto the (R, z)-plane, thus ignoring in the first stage the Galactic azimuthal angle of the stars (although this is considered in Sect. 4.2). We bin the meridional plane as in Fig. 1 and always require at least 100 stars per bin.

3.2. Accounting for measurement errors

Measurement errors affect the observed velocity moments and can therefore have a significant effect on the inferred tilt angles (Siebert et al. 2008). To establish their effect we explore here two "methods" to account for the errors and for recovering the (intrinsic) velocity moments.

Method 1. We assume that the stars in a given spatial bin have similar measurement errors. This assumption is reasonable because the measurement errors in a particular bin are usually much smaller than the intrinsic velocity dispersion. If the measurement errors were exactly the same for all stars in a bin, the intrinsic velocity covariance matrix can be recovered by subtracting the error covariance matrix from the observed velocity covariance matrix. This follows from the fact that convolving a Gaussian distribution with Gaussian distributed measurement errors will again result in a Gaussian with covariance matrix $\mathbf{\Sigma_{obs}} = \mathbf{\Sigma_{intr}} + \mathbf{\Sigma_{error}}$, where $\mathbf{\Sigma_{obs}}$ and $\mathbf{\Sigma_{intr}}$ are the observed and intrinsic covariance matrix of the velocity distribution respectively. In our approximation $\mathbf{\Sigma_{error}} \approx \mathrm{median}\,(\mathbf{\Sigma_{error,i}})$ for

$$\mathbf{\Sigma_{error,i}} = \begin{bmatrix} \mathrm{var}(v_{R,i}) & \mathrm{cov}(v_{R,i}, v_{z,i}) \\ \mathrm{cov}(v_{R,i}, v_{z,i}) & \mathrm{var}(v_{z,i}) \end{bmatrix}, \tag{4}$$

in which the diagonal terms denote the variance error of the corresponding velocity component of star i. Similarly $\mathrm{cov}(v_{R,i}, v_{z,i})$ denotes the error covariance for the (v_R, v_z) measurements of star i. For the required typical errors we take the relevant median errors of the stars in the bin. The recovered intrinsic velocity moments are then used to characterise the velocity distribution. The errors on these moments are analytically estimated and then propagated into uncertainties on the recovered tilt angles. More details can be found in Appendix A.

Method 2. We perform Markov Chain Monte Carlo (MCMC) modelling (Foreman-Mackey et al. 2013) for bins with a smaller number of stars (with $100 < N < 2,000$). This aims to solve for the intrinsic velocity dispersions $\sigma(v_R)_{\rm intr}$ and $\sigma(v_z)_{\rm intr}$, the mean velocities $\langle v_R \rangle$ and $\langle v_z \rangle$, and the covariance term $\mathrm{cov}(v_R, v_z)_{\rm intr}$ in each bin. This is done by maximizing the bivariate Gaussian likelihood function $L = \prod_{i=1}^{N} L_i$, where

$$\begin{aligned} L_i &= L_i[\langle v_R \rangle, \sigma(v_R)_{\rm intr}, \langle v_z \rangle, \sigma(v_z)_{\rm intr}, \mathrm{cov}(v_R, v_z)_{\rm intr}] \\ &= \frac{1}{\sqrt{\det(2\pi\mathbf{\Sigma_i})}} \exp\left[-\frac{1}{2}(\boldsymbol{x_i} - \boldsymbol{\mu})^\intercal \mathbf{\Sigma_i}^{-1} (\boldsymbol{x_i} - \boldsymbol{\mu})\right], \end{aligned} \tag{5}$$

in which $\boldsymbol{x_i} = [v_{R,i}, v_{z,i}]$, $\boldsymbol{\mu} = [\langle v_R \rangle, \langle v_z \rangle]$ and $\mathbf{\Sigma_i} = \mathbf{\Sigma_{intr}} + \mathbf{\Sigma_{error,i}}$. Whereas in *Method 1* $\mathbf{\Sigma_{error,i}}$ was assumed to be the same for each star, we here use $\mathbf{\Sigma_{error,i}}$ for each star separately. We add priors to the model that only allow for positive velocity dispersions in v_R and v_z and that restrict the correlation between v_R and v_z always to be within [−1,1]. For a given bin, the samples drawn by the MCMC run translate into a distribution of tilt angles. We take the median as the best estimate of the tilt angle. For its error we take half the difference between the tilt angles corresponding to the 16$^{\rm th}$ and 84$^{\rm th}$ percentile.

In general we find that the effect of the measurement errors on the recovered moments is small. Moreover, for most bins the velocity measurement errors are sufficiently similar and small that we may use the computationally much faster *Method 1* instead of the MCMC-based deconvolution. We have also compared the results to the case in which we simply compute the variances of the observed stellar velocities in the bins of interest, and take these at face value, i.e. we do not take into account the measurement errors. The results are again rather similar, see for example, Fig. A.1 of Appendix A which shows the distributions of the measurement errors for the bin located at $R = 13.0$ kpc and $z = 1.5$ kpc. Therefore in what follows, we use the results from *Method 1* unless stated otherwise.

4. Results

We present our measurement of the tilt angles by showing velocity ellipses in the meridional plane. At each position (R, z),

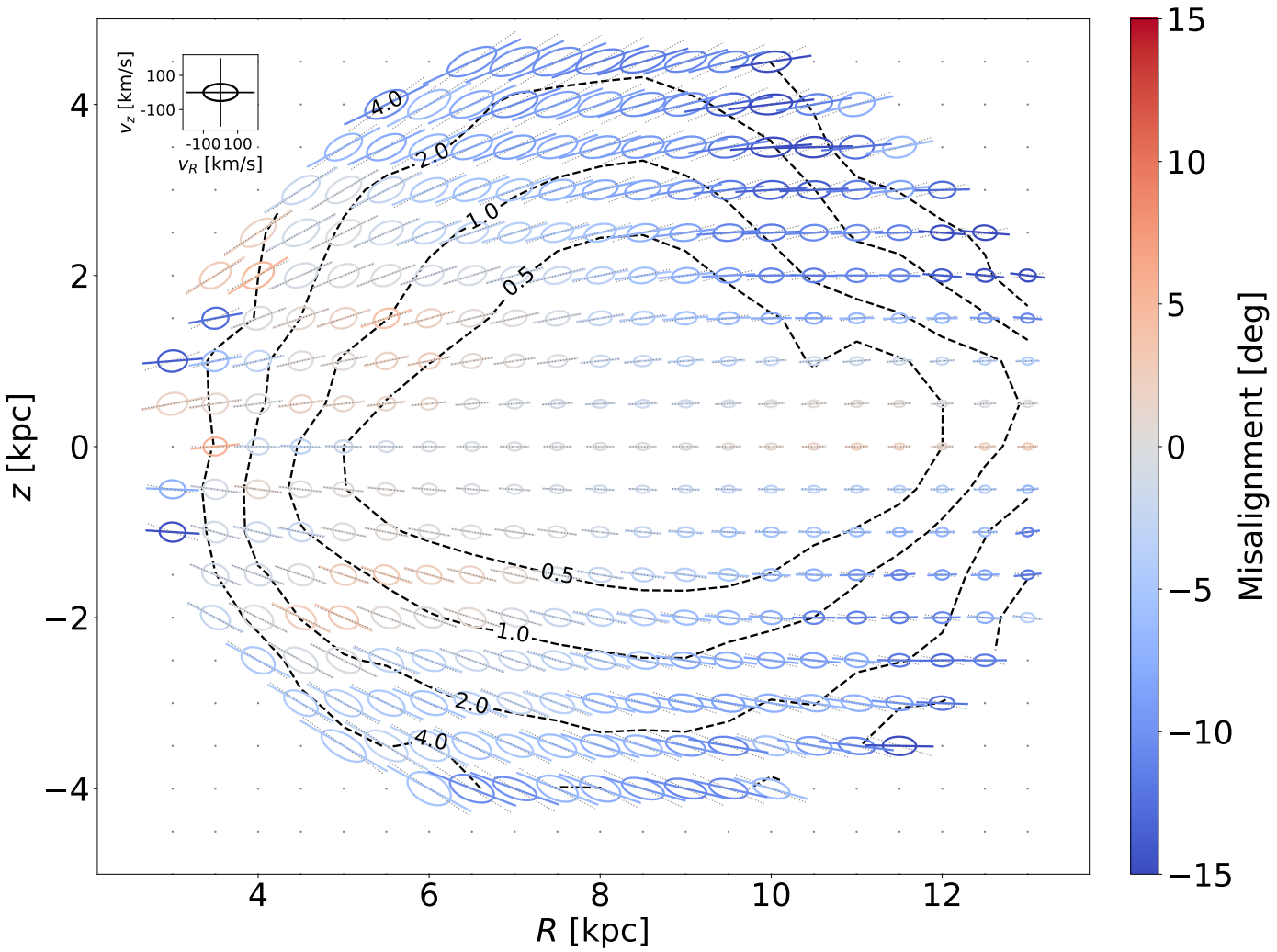

Fig. 2. Velocity ellipses in the meridional plane. The ellipses are colour-coded by their misalignment with respect to spherical alignment. The orientation that corresponds to spherical alignment is indicated by the dotted grey line through each ellipse. For $4 \lesssim R \lesssim 7$ kpc, the ellipses are consistent with spherical alignment up to about 2 kpc in Galactic height. For $R \sim 12$ kpc the ellipses are consistent with close to cylindrical alignment for almost all heights probed. The inset in the top left of the figure shows the velocity ellipse for a non-tilted distribution with dispersions $\sigma(v_R) = 100$ km/s and $\sigma(v_z) = 50$ km/s (see Sect. 4 for more information). The contours show the (relatively small) errors on the recovered tilt angles and are drawn for error levels of $[0.5, 1.0, 2.0, 4.0]$ degrees.

we define a set of axes with v_R into the R-direction and v_z in the z-direction. The centre of each velocity ellipse is always placed at its position (R, z). The size of the major and minor axis of each ellipse scale with the intrinsic velocity dispersions along these directions. The R- and z-axis are both scaled by the same constant c_x. Similarly, all v_R- and v_z-axes are scaled by a constant c_v, thus both sets of axes have an aspect ratio of 1. As a consequence, the velocity ellipses drawn will actually point to the Galactic centre when there is spherical alignment. As a reference, the inset in the figures shows a velocity distribution aligned in cylindrical coordinates and with $\sigma(v_R) = 100$ km/s and $\sigma(v_z) = 50$ km/s (unless stated otherwise).

4.1. Tilt angles projected onto the (R, z)-plane

Fig. 2 shows the velocity ellipses colour-coded by their angular misalignment with respect to spherical alignment. For $z \geq 0$ kpc we define the misalignment as $\gamma - \gamma_{\rm sph}$, whereas for $z < 0$ kpc the misalignment is $\gamma_{\rm sph} - \gamma$. Steeper tilt angles result in positive misalignment (from light to dark red), shallower tilt angles in negative misalignment (from light to dark blue). Ellipses that are consistent with spherical alignment are greyish. At the midplane it is however not possible to distinguish between spherical and cylindrical alignment, since both $\gamma_{\rm sph} = \gamma_{\rm cyl} = 0°$ at $z = 0$ kpc, thus consistency with spherical alignment here also implies consistency with cylindrical alignment. Only away from the midplane it is possible to differentiate between these types of alignment. From this figure it is evident that there are (almost) no bins that have alignments much steeper than spherical alignment (i.e. there are no dark red ellipses, only a few light red ones). In the inner regions of the Galaxy ($R \sim 4$ kpc) the tilt angles have the steepest gradients with respect to z as would be expected for spherical alignment. At $R > 8$ kpc and $|z| \gtrsim 1$ kpc, the ellipses have a negative misalignment. Contours of constant error values on the recovered tilt angles are added in Fig. 2. We have drawn contours for errors reaching 0.5, 1.0, 2.0, and 4.0 degrees. These contours show the great quality of our dataset over the distance range explored.

To be able to assess whether the tilt angles found are consistent with spherical or cylindrical alignment we show them with

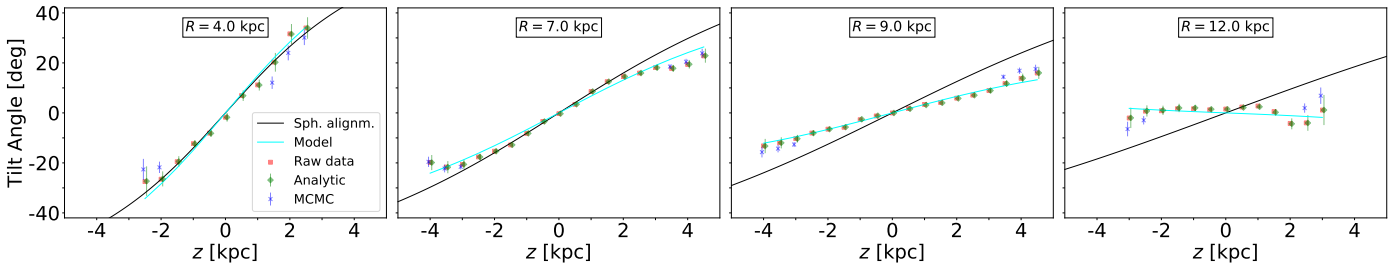

Fig. 3. Tilt angles as a function of Galactic height for different positions across the Galaxy. We show the trends with z for $R = [4, 7, 9, 12]$ kpc. The red squares, green diamonds, and blue crosses are based on the methods described in Sect. 3.2 (see text). They give consistent results given the error bars. The solid black line shows the trend that would correspond to spherical alignment. The tilt angle is clearly changing from spherical alignment in the inner Galaxy ($R \sim 4$ kpc) towards cylindrical alignment at $R \sim 12$ kpc. The cyan line shows the analytic description of the data as proposed in Sect. 4.4.

error bars in Fig. 3 as a function of height for four Galactic radii, namely $R = [4, 7, 9, 12]$ kpc. The red squares (without error bars; labelled 'Raw data'), follow from computing the moments directly from the data, the green diamonds ('Analytic'), are derived using *Method 1* for accounting for the measurement errors and the blue crosses (labelled 'MCMC') are based on *Method 2* (and are only computed for bins with $100 < N < 2,000$, see Sect. 3.2). Typically, the different methods yield consistent values for the tilt angles as well as for the uncertainties on these.

The black curve in Fig. 3 shows the expectation in the case of spherical alignment. It is clear that at $R = 4$ kpc (left panel) the recovered tilt angles are fully in agreement with spherical alignment for all heights explored. At $R = 7$ kpc (left center panel) the data is only consistent with spherical alignment up to $|z| \sim 2$ kpc. For $|z| \gtrsim 2$ kpc the tilt angles are not as steep. For $R = 9$ the tilt angles are neither consistent with spherical alignment for $|z| \gtrsim 1$ kpc, nor consistent with cylindrical alignment. Finally, for $R = 12$ kpc the orientation of the ellipses become consistent with cylindrical alignment for all heights probed (with the exception of the bin at $z = +2$ kpc) and inconsistent with spherical alignment for $|z| \gtrsim 1$ kpc.

4.2. Tilt angles for different azimuthal angles

Since the Galaxy is not axisymmetric we now investigate whether the tilt angles vary with azimuth by taking into account the 3D location of the individual stars in our dataset. We bin the data into cartesian bins (x, y, z) whose volume is fixed to $1{\times}1{\times}1$ kpc^3, which implies that the different azimuthal cones we explore contain independent data for $R > 4$ kpc. These cones are centered on three different angles $\phi = [165°, 180°, 195°]$.

The resulting maps are shown in Fig. 4. Since the data is effectively sliced in ϕ, the number of stars at a given (R, z) is lower and as a consequence the spatial bins cover a lower spatial extent in comparison to Sect. 4.1. A coarse comparison of the different panels in this figure suggests that the variations with azimuth are small.

Some of these differences can be seen more clearly in Fig. 5, for specific radii $R = [5, 7, 9, 11]$ kpc. Here the different symbols, namely red squares, green diamonds, and blue crosses correspond to the measurements for $\phi = [165°, 180°, 195°]$, respectively. The black starred symbols show the measurements from all stars at given R and z and irrespective of azimuth (as in Sect. 4.1). At $R = 5$ kpc and at $z \sim -2$ kpc the tilt angles become less steep with increasing ϕ and an opposite trend might be present at larger heights above the midplane. At (R, z, ϕ) = (8 kpc, +2.5 kpc, $\phi = 195°$) the recovered tilt angles are consistent with cylindrical alignment, albeit with relatively large error

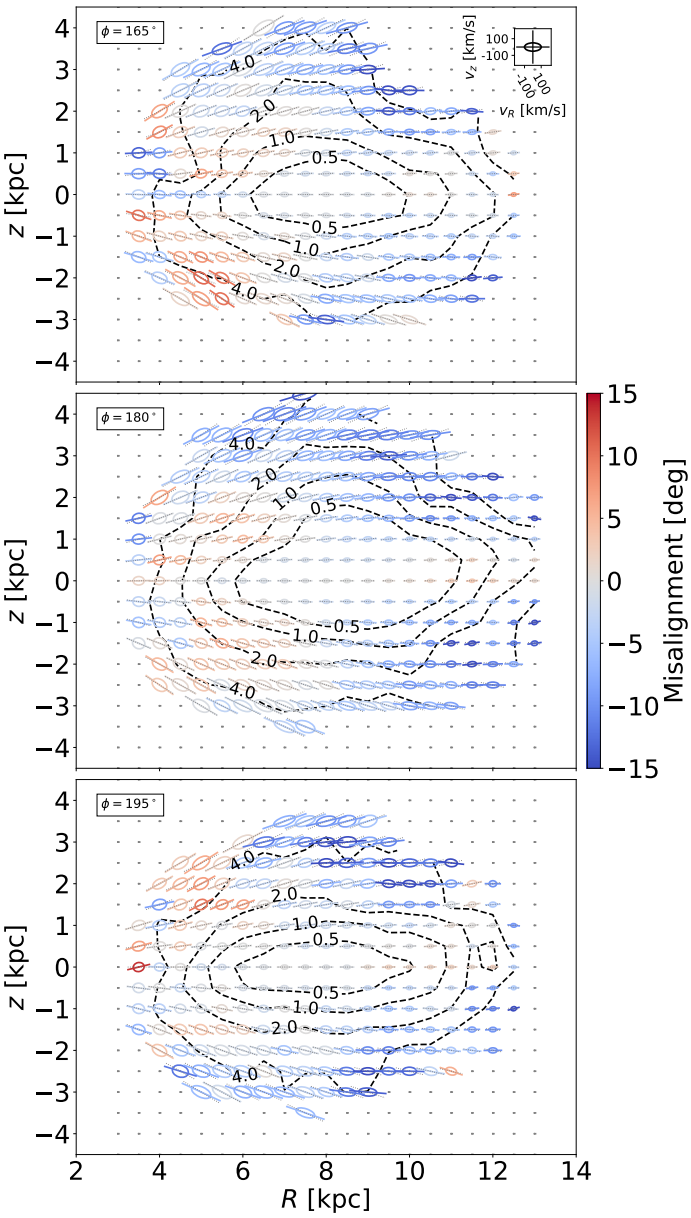

Fig. 4. The tilt of the velocity ellipses in the meridional plane, now for different positions in azimuth ($\phi = [165°, 180°, 195°]$ from top to bottom, respectively). The spatial bins are cubes in (x, y, z), of 1 kpc on a side. The colours of the ellipses represent the misalignment with respect to spherical alignment (as in Fig. 2).

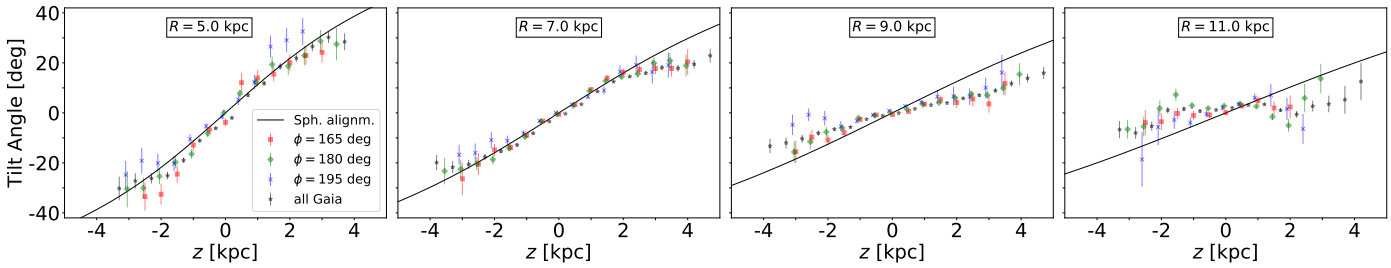

Fig. 5. Tilt angles as a function of Galactic height for different radial and azimuthal positions across the Galaxy. The red squares, green diamonds, and blue crosses show the measurements for $\phi = [165°, 180°, 195°]$, respectively. The black starred symbols show the measurements irrespective of azimuth (as in Sect. 4.1). The figure shows that the tilt angles for different azimuths are fairly consistent with each other given the error bars. The solid black line denotes the trend expected for spherical alignment.

bars, and deviate from those at $\phi = 165°$ and $\phi = 180°$, for which the alignment is closer to spherical. Similarly, at $R = 9$ kpc and $z \sim -2.5$ kpc the tilt angles for $\phi = 195°$ are more or less consistent with cylindrical alignment, whereas the other azimuths tend to indicate tilt angles much closer to spherical alignment.

We conclude that, even though some bins reveal slightly different tilt angles for different azimuths, the overall qualitative trends are very similar to the case in which we projected all stars onto the (R, z)-plane, thus justifying the approach used in Sect. 4.1. These results also suggest that the degree of non-axisymmetry, in terms of the tilt angles, is modest over the azimuthal range explored.

4.3. Variations with stellar populations

In this section we explore whether different populations of stars follow similar trends in tilt angle. Since *Gaia* DR2 does not provide metallicity information we use metallicities from LAMOST DR4. The dataset from this cross-match is much larger than those obtained using RAVE or APOGEE, which allows us to compare the tilt angles as a function of metallicity over a significantly larger region. Note that we refrain from merging with the RAVE and APOGEE datasets to avoid possible offsets between metallicity scales in the different surveys. Only stars with metallicity uncertainties up to 0.2 dex are considered in our analysis.

We proceed to classify the stars according to a halo population, defined by [M/H] < -1.0 dex, a thick disk population by $-1.0 <$ [M/H] < -0.5 dex, and a thin disk population by [M/H] > -0.4 dex. With these criteria, our sample contains 24, 297 halo stars, the thick disk is represented by 268, 145 stars, and the thin disk by 1, 962, 313 stars.

Fig. 6 shows the velocity ellipsoids and tilt angles as a function of position in the meridional plane for the halo (left), thick disk (middle) and thin disk (right) subsamples. Notice the different spatial coverage of the subsets, which reflects differences in the number of stars (recall that to reliably measure a tilt angle we require at least 100 stars in a spatial bin). Note as well how much larger the ellipses are for the halo population compared to those of the thick and thin disks. In fact, we have had to use different scales for the panels: the insets in the bottom right of each panel show ellipses whose semi-major and semi-minor axes correspond to dispersions of $\sigma(v_R) = 200$ km/s and $\sigma(v_z) = 100$ km/s for the halo and thick disk populations, and to $\sigma(v_R) = 100$ km/s and $\sigma(v_z) = 50$ km/s for the thin disk.

As in previous sections, the colours in Fig. 6 represent the misalignment of the tilt angles with respect to spherical alignment. Notice that the same trends as found earlier are now visible for each population independently: at $R \lesssim 7$ kpc the alignment is closer to spherical, while from $R = 10$ kpc to $R = 12$ kpc the behaviour turns towards close to cylindrical alignment. This is even clearer when comparing the tilt angles derived for each population at specific radii, as shown in Fig. 7. Therefore we may conclude that the results shown in Sect. 4.1 are not dependent on the different populations present throughout the volume probed by our dataset.

4.4. Quantifying the degree of spherical alignment

Because the trends seen in the tilt angles are not strongly dependent on Galactic azimuth nor on stellar population, we here aim to provide a simple description of their variation with radius R and height z as found in Sect. 4.1.

Since we infer near spherical alignment for $R \lesssim 6$ kpc, we consider expanding α around a point (R_0, z_0):

$$\begin{aligned}\alpha(R,z) = \alpha(R_0,z_0) &+ a_1\,(R-R_0) + a_2\,(z-z_0)\\ &+ a_3\,(R-R_0)(z-z_0)\\ &+ a_4\,(R-R_0)^2 + a_5\,(z-z_0)^2 + \ldots\ ,\end{aligned} \tag{6}$$

where a_i are constants and both R and z in kpc. By definition $\alpha(R_0, z_0) = 0°$. We further set $z_0 = 0$ kpc (i.e. the symmetry plane of α is set to be the Galactic midplane). Moreover, $a_1 = a_4 = 0$, since for most realistic models the tilt angle does not vary at the midplane. By symmetry arguments the coefficients of all even powers of z (including a_5) must be zero, since α is expected to be either antisymmetric with respect to the midplane or zero. Since we have found that at $R \sim 4-5$ kpc the tilt angles are consistent with spherical alignment for all z probed (see left panel of Fig. 3), we additionally set $a_2 = 0$ such that at $R = R_0$: $\alpha(R_0, z) = 0°$. With these choices:

$$\alpha(R,z) \approx a_3\,(R-R_0)z\,. \tag{7}$$

We thus fit this functional form to the data to derive values for R_0 and a_3 such that the χ^2-statistic defined as:

$$\chi^2 = \sum_{i=1}^{N_{\rm bins}} \left(\frac{\alpha(R_i,z_i)_{\rm model} - \alpha(R_i,z_i)_{\rm obs}}{\epsilon[\alpha(R_i,z_i)_{\rm obs}]} \right)^2 . \tag{8}$$

is minimized. Here i runs over the number of bins $N_{\rm bins}$ where a measurement is made, i.e. where $N > 100$ stars.

For most bins at $|z| \leq 2.0$ kpc and $5 \leq R \leq 12$ kpc the inferred statistical errors on the tilt angles are very small (e.g. see the dashed contours in Fig. 2). In that case, systematic errors need to be considered. One such source of systematic errors are substructures. We performed tests to estimate the effect of substructures in velocity space on the tilt angle. To this end we inserted $N_{\rm sub} = 1$, 4, 9, 16, 25, or 36 substructures on smooth

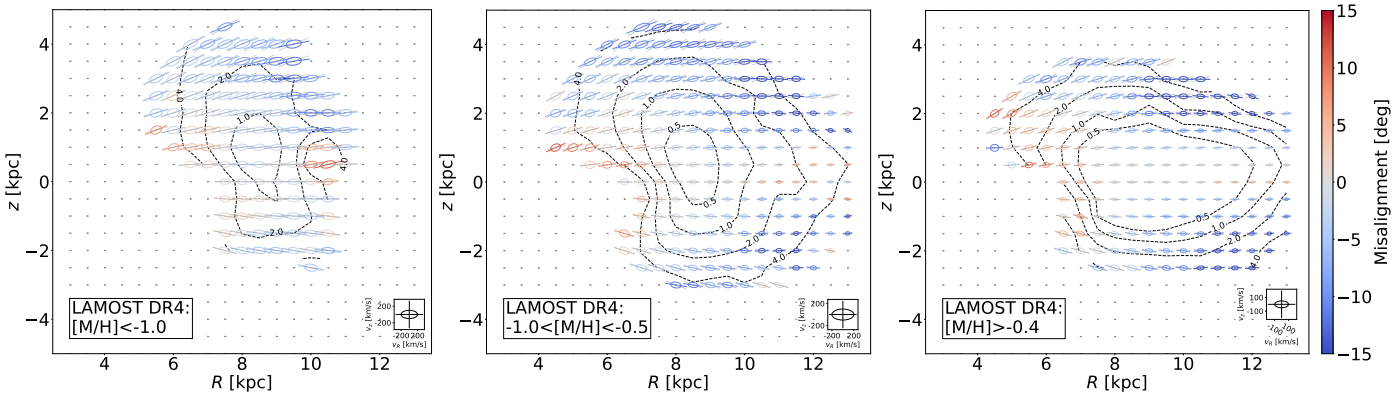

Fig. 6. Velocity ellipses in the meridional plane, as in Fig. 2, but now for the subsamples representing halo (left), thick disk (middle) and thin disk (right) populations. Note that the scaling of the velocity ellipses, indicated by the insets in the bottom right of each panel, are different. The colour coding of the ellipses represents the misalignment with respect to spherical alignment and is the same as in Fig. 2. There is no strong evidence that the tilt angles of the different populations behave differently.

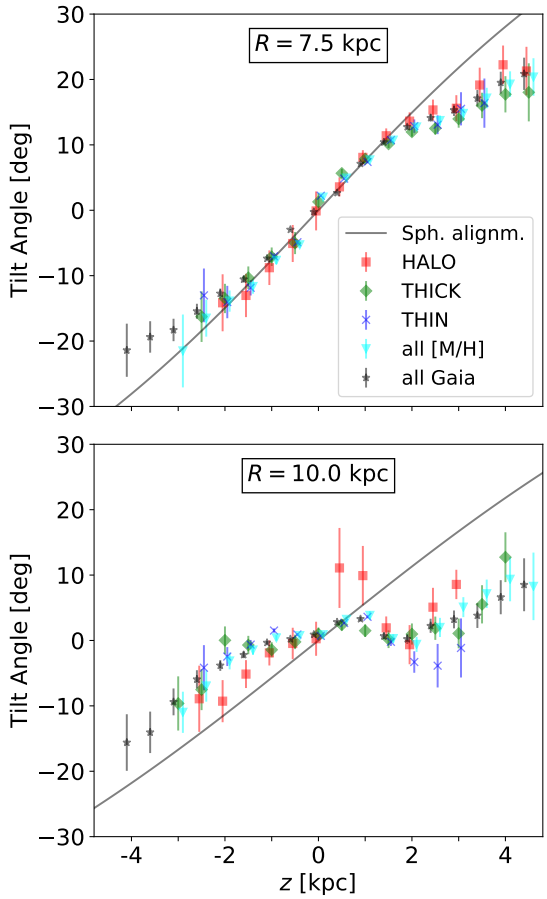

Fig. 7. Tilt angles as a function of Galactic height for different populations of stars. We show the trends with z for $R = 7.5$ (top) and $R = 10$ kpc (bottom). The red squares, green diamonds, and blue crosses show the results for the halo, thick, and thin disk population described in Sect. 4.3, respectively. The light blue triangles correspond to all LAMOST stars with metallicity information with uncertainties smaller than 0.2 dex, while the black stars are for all stars regardless of whether or not they have metallicity information (as in Sect. 4.1). The solid black line shows the trend that would correspond to spherical alignment.

non-tilted velocity distributions with velocity dispersions of 20 and 35 km/s in v_z and v_R (i.e. values representative of the thin disk near $R \sim R_\odot$), respectively. Each substructure was assigned a random number of stars such that the total fraction of stars in substructures is $f_{\rm sub} = 5$, 10, 15, or 20%. We randomly assigned velocity dispersions to the substructures, drawn uniformly from 1 to 5 km/s in both directions. For each combination of ($N_{\rm sub}$, $f_{\rm sub}$) we considered 100 realizations. The median (absolute) tilt angle found from these experiments is ~ 1 degree, implying that this value is representative of the error introduced by neglecting the presence of substructures in a velocity distribution. This result is independent of the total number of stars N for $N \gtrsim 10000$ (a value that is representative of the number of stars in the bins with $\epsilon[\alpha(R_i, z_i)] < 1°$). Thus, when minimizing the χ^2 we consider a floor for the statistical error $\epsilon[\alpha(R_i, z_i)]$ in each bin of 1°.

We fit to find $R_0 = (5.18 \pm 0.10)$ kpc and $a_3 = (0.774 \pm 0.023)°/\mathrm{kpc}^2$ resulting in a reduced χ^2 of 2.07. The cyan line in Fig. 3 shows the tilt angles predicted by this fit, which reproduces relatively well the trends observed in the data. The model goes through the 1σ-error bars for approximately 50% of all spatial bins, while for 97% of bins the model matches the data within 3× the estimated uncertainty. This indicates that our simple model provides a fair description of the behaviour of the tilt of the velocity ellipsoid across the Galactic volume probed by our dataset.

The total reduced χ^2-value is large because of some bins with small measurement errors which do not exactly match the model. For example, at $R = 4.5$ and $z = 0$ kpc we measure from the data $\gamma = (-3.2 \pm 0.9)°$, whereas the model inevitably goes through 0.0°. Also, at $R = 3$ kpc the observed tilt angles tend to be more consistent with (close to) cylindrical alignment, whereas the fitted model has not enough freedom to fit this behaviour. Furthermore, at $R \sim 10.0$ kpc the tilt angles are asymmetric with respect to the $z = 0$ plane: at $z > 0$ kpc they more or less attain a constant value of $\sim 2.0°$, whereas below the midplane the tilt angles become steeper with z (e.g. $-10°$ at $z = -3.0$ kpc). The fits at these radii are therefore relatively poor. For the bins between $R = 11$ and $R = 13$ kpc, we notice that for $|z| \lesssim 1$ kpc the observed tilt angles seem to have a small positive offset from zero. These offsets are small (of order 2 degrees), although they do affect the goodness of fit measure.

5. Discussion

5.1. The impact of the parallax uncertainties on the recovered tilt angles.

Gaia Collaboration et al. (2018a) have reported the presence of a systematic error on the *Gaia* DR2 parallaxes in the form of a zero-point offset, of a few 10 of μas and whose exact amplitude depends on location on the sky. This systematic zero-point offset implies that the (tangential) velocities of more distant stars may not be fully correct. In this section we estimate the impact on the recovered tilt angles induced by this systematic error while also including the effects of random errors[1]. Their effect is examined by using the *Gaia* Universe Model Snapshot (GUMS, Robin et al. 2012), which is based on the Besançon Galaxy Model (Robin et al. 2003). We mimic the *Gaia* DR2 subsample with full phase-space information, by selecting stars in GUMS that have $G < 13$ mag, as this is roughly the magnitude limit for radial velocities in *Gaia*'s current data release.

The observables in the GUMS catalog are error-free. We generate 100 data realizations by convolving the GUMS sample with a Gaussian with *Gaia* DR2-like random errors for the parallaxes (Gaia Collaboration et al. 2016b; Veljanoski et al. 2019). We similarly add systematic parallax errors to the sample. The systematic parallax offsets for the stars are drawn from a Gaussian with mean -29μas and standard deviation of 30μas (Lindegren et al. 2018). In each realization we consider only those stars that satisfy $\varpi/\epsilon(\varpi) > 5$ and $\varpi \gtrsim 200\mu$as. Here ϖ is the observed parallax and $\epsilon(\varpi)$ the random parallax error and thus the same quality criteria are applied as to the real data (see Sect. 2).

For each spatial bin the median of the distribution of tilt angles (recovered from the different realizations) is compared to the tilt angles from the error-free model, on the meridional plane. The error-free GUMS model has close to cylindrically aligned velocity ellipses. The impact of the parallax uncertainties on the tilt angles depends on location as can be seen in Fig. 8. At $R \lesssim 7$ kpc the orientations of the velocity ellipses change towards the direction of spherical alignment ($\Delta\gamma_{\rm GUMS} > 0$ for $z > 0$ and $\Delta\gamma_{\rm GUMS} < 0$ for $z < 0$), while for $R \gtrsim 9$ kpc the change is in the opposite sense.

In the context of *Gaia* DR2, these findings imply that spherical alignment can be enhanced in the inner Galaxy, while trends towards cylindrical alignment can be enhanced for the outer Galaxy. If we take the results from GUMS at face value, $|\Delta\gamma_{\rm GUMS}| \approx 6^\circ$ at $(R, |z|) \sim (5, 3)$ kpc, which is too small to change the type of alignment at this location (where we had estimated $\gamma \sim 30^\circ$). On the other hand for $(R, |z|) \sim (12, 2)$ kpc we find that $|\Delta\gamma_{\rm GUMS}|$ ranges from 3 to 7°, whereas $|\gamma_{\rm sph}| = 9.5^\circ$. At the spatial boundaries of our dataset the changes induced by the parallax uncertainties can even reach $\sim 10^\circ$. We find similar amplitudes for the cases explored in Appendix B (starting from spherical or cylindrically aligned ellipsoids).

These findings may explain the negative tilt angle found above the midplane and positive below the midplane at $R \sim 13$ kpc, as being due to errors on an intrinsically cylindrically aligned velocity ellipsoid. The estimated parallax effects are generally non-negligible when trying to differentiate between spherical and cylindrical alignment for $R \gtrsim 10$ kpc and $|z| \lesssim 2$ kpc, since here $|\gamma_{\rm sph}|$ is generally small compared to the possible systematics described in this Section. Within the distance range of 5 kpc considered, the effect of a parallax zero-point offset however does not seem strong enough to make the observed tilt angles fully consistent with spherical alignment.

[1] In Appendix B we analytically compute how the v_R- and v_Z-velocities (and thus their moments and tilt angles) are affected by the parallax zero-point offset alone.

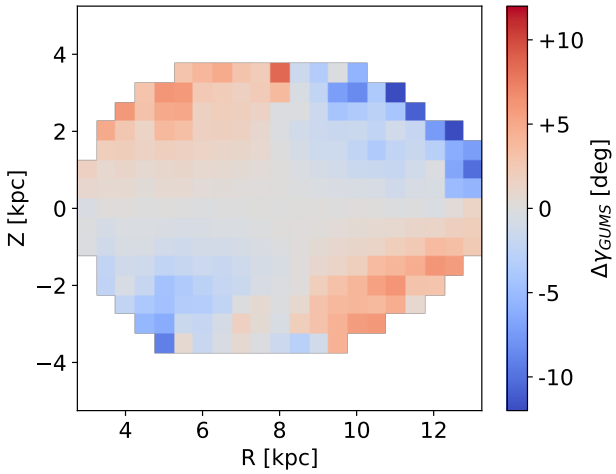

Fig. 8. Differences in tilt angles, $\Delta\gamma_{\rm GUMS}$ in degrees, between parallax error convolved realizations and the error-free GUMS catalog. At each spatial bin the median tilt angle is measured for 100 data realizations. In each realization both random and systematic errors are taken into account for the parallaxes of the stars.

5.2. Constraints to mass models of the Milky Way

Several mass models of the Milky Way have been proposed by matching a variety of constraints (e.g. McMillan 2011; Piffl et al. 2014; McMillan 2017). Particularly useful for the interpretation of the findings reported in this paper are Stäckel models. For example, Famaey & Dejonghe (2003) have extended the two-Stäckel component work of Batsleer & Dejonghe (1994) by adding a third component, such that the model could allow for a thin and thick disk, in addition to a halo component. The authors use constraints such as the (flat) rotation curve, circular velocity at the position of the Sun, the Oort constants, and the local total mass density in the disk to search for a set of consistent parameters for their Stäckel models.

Axisymmetric models with a potential of Stäckel form (also see: de Zeeuw 1985; Dejonghe & de Zeeuw 1988) have the property that the equations of motions are separable in their spheroidal coordinates. Therefore the principal axes of the velocity ellipsoids are always aligned with these coordinates. The foci of such a coordinate system then determine the alignment at each position. For a composite model to be of a Stäckel form, the locations of the foci must be identical for all components.

As an example we take the set of prolate spheroidal coordinates, (λ, ϕ, ν), from Famaey & Dejonghe (2003, mass model II). The foci of this oblate mass model are located at $(R, z) = (0, \pm 0.88)$ kpc. At $R \sim 0$ and $|z| \lesssim 0.88$ kpc such spheroidal coordinates align with the cylindrical coordinate system (see Fig. 9). Outside of these foci and with increasing distance from the Galactic centre the spheroidal coordinates approach the spherical coordinate system. In general any (composite) Stäckel model will predict a change in the tilt of the velocity ellipse from cylindrical to spherical alignment. The transition radius depends on the location of the foci.

Since the observed tilt angles at $R \sim 4$ kpc already show near spherical alignment, this implies foci at $|z| \lesssim 4$ kpc. Their exact position would depend on whether the innermost region of the Galaxy, not probed by our dataset, is cylindrically aligned

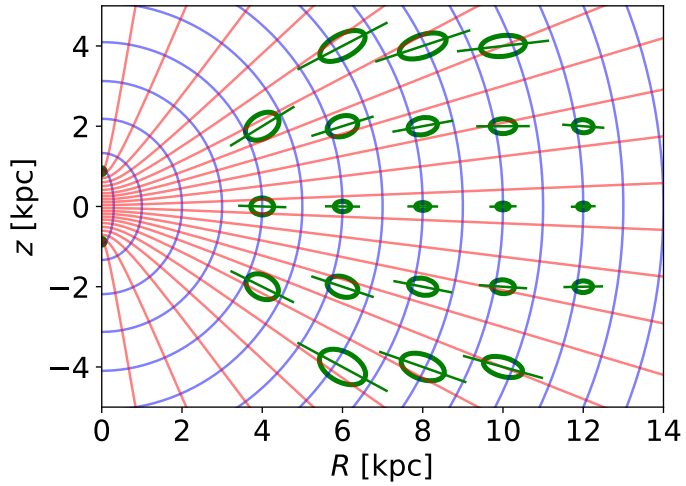

Fig. 9. Contours of constant prolate spheroidal coordinates, (λ, ν), with foci at $R = 0$ and $z = \pm 0.88$ kpc (see text). Contours of constant λ are shown in blue, contours of constant ν in red. The green ellipses show some of our measured velocity ellipses (*Method 1*). Their orientation does not align with the coordinate contours at $R \gtrsim 8$ kpc and $|z| \gtrsim 2$ kpc.

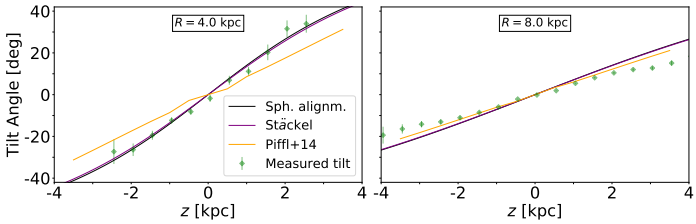

Fig. 10. Tilt angles for both the Stäckel (purple line) and Piffl+14 (orange line) model for radii at $R = 4$ and $R = 8$ kpc (see text). For comparison we add our measurement as green diamonds (*Method 1*).

or not, and if so at what distance the transition occurs. However, the tilt angles in the outer Galaxy ($9 \lesssim R \lesssim 12$ kpc) are not consistent with Stäckel models that have foci at $|z| \lesssim 4$ kpc. A Stäckel component with a large focal distance could produce cylindrical alignment up to these outer regions, but would consequently not be consistent with the near spherical alignment found for $4 \lesssim R \lesssim 7$ kpc. We have numerically checked both statements by comparing the predicted tilt angles of both oblate and prolate Stäckel models (for a large range of different focal distances) to the observed tilt angles while taking into account their errors. A model in which a Stäckel potential with a small focal distance dominates the inner Galaxy ($R \lesssim 7$ kpc) and in which a Stäckel component with a large focal distance dominates the outer Galaxy ($R \gtrsim 9$ kpc) could be consistent with the trend seen. Unfortunately, the superposition of multiple Stäckel components with different foci will not be of a Stäckel form.

There are of course many more models with bulge, disk and halo components (e.g. spherical bulge, exponential disk, Navarro-Frenk-White (NFW, Navarro et al. 1996) halo or Miyamoto & Nagai (1975) models). The separable models are in that sense a subset but have the advantage that for them the tilt of the velocity ellipsoid is dictated by the coordinate system in which the equations of motion (Hamilton-Jacobi equation to be more precise) separate.

Piffl et al. (2014) have applied a five component mass model (gas disk, thin and thick disk, flattened bulge and dark halo) to RAVE DR4 stars. Using their best-fitting parameters we computed the relevant velocity moments from the distribution function for a similar range in R and z as probed in our dataset. The tilt angles for this model are spherically aligned for $R \gtrsim 7$ kpc and are, as in the separable models discussed above, changing towards cylindrical alignment with decreasing R and therefore this model suffers the same problems as the composite Stäckel model described above.

In Fig. 10 we show the tilt angles for both the Stäckel model (purple line) of Famaey & Dejonghe (2003) and the Piffl et al. (2014) model (orange line), for radii $R = 4$ and $R = 8$ kpc. The green diamonds indicate the tilt angles as found by *Method 1*. Since this Stäckel model has focii at $|z| \lesssim 0.88$, which is very close to the Galactic centre with respect to the innermost radius probed in our dataset, the Stäckel model is almost indistinguishable from spherical alignment for all positions probed. The Piffl+14 model has tilt angles that are shallower at $R = 4$ kpc, but also approaches spherical alignment with increasing Galactic radius. As an example, the tilt angles from the Piffl+14 model at $R = 8$ kpc are seen to nearly coincide with the expectation for spherical alignment.

6. Conclusions

We have studied the trends in the tilt angle of the velocity ellipsoids in the meridional plane for a high quality sample of 8.5 million stars located across a large portion of the Galaxy, from $R \sim 3$ to 13 kpc, and reaching a maximum distance from the plane of ~ 4 kpc. Approximately 73% of the stars in our sample stem from the 6-d subset of *Gaia* DR2, while the remaining 27% are from the cross-match between the full 5-d *Gaia* DR2 and LAMOST DR4, APOGEE DR14, or RAVE DR5, surveys that provide the missing line-of-sight velocity information.

We find that the tilt angles are consistent with (near) spherical alignment at $R \sim (4 - 5)$ kpc for all heights probed ($|z| \lesssim 3$ kpc). At $R \sim 7$ kpc the consistency remains up to $|z| \sim 2$ kpc, beyond which the tilt angles are clearly shallower than spherical. At $R \sim 12$ kpc the tilt angles are consistent with (close to) cylindrical alignment up to the heights probed ($|z| \leq 3$ kpc) and inconsistent with spherical alignment for $|z| \gtrsim 1$ kpc. These trends remain when the stars are separated into "populations" according to their metallicity (as given by LAMOST DR4). We provide a simple analytic function, $\alpha(R, z) \approx 0.774(R - 5.18)z$, that fits well the trend in tilt angle (in degrees and as defined in the spherical coordinate system) as a function of Galactic radius and height, after projecting the stars onto the (R, z)-plane.

We have explored how the (systematic) astrometric parallax errors from *Gaia* DR2 affect our estimates of the tilt angle. We find that at large distances from the Sun ($d > 3$ kpc) an effect is present but that it is only of sufficient amplitude towards the outer Galaxy (for $R \gtrsim 10$ kpc and $|z| > 2$ kpc). In these regions, the angles tend to become shallower (i.e. more cylindrically aligned if the ellipsoid is intrinsically spherically aligned). This implies that only near the outer edge of the sample our measurements may be subject to a bias, and that the trends found (from spherical alignment towards the inner Galaxy to shallower at larger distances from the Galactic centre) are robust.

In comparison to previous measurements of the tilt angle at the Solar radius by Binney et al. (2014) and Büdenbender et al. (2015), we find it to be less spherically aligned. The more recent work by Wegg et al. (2018) based on RR Lyrae stars probes distances between 1.5 and 20 kpc from the Galactic centre and is therefore complementary to ours since the outer spatial boundary of our sample roughly coincides with the inner spatial boundary of their dataset. Note however that we use a 6-d sample while

they only have 5-d information. Wegg et al. (2018) find near spherical alignment for $r \gtrsim 5$ kpc at $|z| \gtrsim 3$ kpc, in agreement with our measurements for $R \sim 5$ kpc up to the heights probed by our sample ($|z| \lesssim 3$ kpc). These authors also find indications that for their innermost radii and Galactic heights the tilt angles do become shallower, confirming our findings that not only at the innermost radius probed ($R = 3.5$ kpc), but also for $R \gtrsim 7$ the velocity ellipsoid is more cylindrically aligned (up to the heights probed by our sample).

Mass models of the Milky Way should be consistent with the measured tilt angles. We have compared our estimates and trends in the tilt angles with those expected for a composite Stäckel potential that has been used to describe the Milky Way (Famaey & Dejonghe 2003). We find that this (and any oblate) Stäckel potential will tend to predict cylindrical alignment in the inner Galaxy and spherical alignment in the outer Galaxy, which seems to be in conflict with our findings. This is also the case for a multi-component potential by Piffl et al. (2014) indicating that further development of dynamical models will be necessary to underpin the mass distribution in our Galaxy.

Another step will be to consider the correlations between all velocity components, i.e. including v_ϕ, which is already possible with the same *Gaia* DR2 catalog. The interpretation of these correlations are directly related to non-axisymmetries, requires more sophisticated modelling (e.g. Hunt et al. 2018; Quillen et al. 2018; Sellwood et al. 2019), and will be of interest in future work.

Acknowledgements. JH thanks Helmer Koppelman for helping in creating the dataset used in this work (Koppelman et al. 2018). AH acknowledges financial support from a VICI grant from the Netherlands Organisation for Scientific Research, N.W.O. TdZ is grateful to the Kapteyn Astronomical Institute for the hospitality during his Blaauw Professorship. This work has made use of data from the European Space Agency (ESA) mission *Gaia* (`https://www.cosmos.esa.int/gaia`), processed by the *Gaia* Data Processing and Analysis Consortium (DPAC, `https://www.cosmos.esa.int/web/gaia/dpac/consortium`). Funding for the DPAC has been provided by national institutions, in particular the institutions participating in the *Gaia* Multilateral Agreement. We have also made use of data from: (1) the APOGEE survey, which is part of Sloan Digital Sky Survey IV. SDSS-IV is managed by the Astrophysical Research Consortium for the Participating Institutions of the SDSS Collaboration (`http://www.sdss.org`). (2) the RAVE survey (`http://www.rave-survey.org`), whose funding has been provided by institutions of the RAVE participants and by their national funding agencies. (3) the LAMOST survey (`www.lamost.org`), funded by the National Development and Reform Commission. LAMOST is operated and managed by the National Astronomical Observatories, Chinese Academy of Sciences. For the analysis, the following software packages have been used: vaex (Breddels & Veljanoski 2018), NumPy (Oliphant 2015), matplotlib (Hunter 2007), Jupyter Notebook (Kluyver et al. 2016), TOPCAT and STILTS (Taylor 2005, 2006).

References

Abazajian, K. N., Adelman-McCarthy, J. K., Agüeros, M. A., et al. 2009, ApJS, 182, 543
An, J. & Evans, N. W. 2016, ApJ, 816, 35
Antoja, T., Figueras, F., Fernández, D., & Torra, J. 2008, A&A, 490, 135
Antoja, T., Helmi, A., Romero-Gómez, M., et al. 2018, Nature, 561, 360
Arenou, F., Luri, X., Babusiaux, C., et al. 2018, A&A, 616, A17
Batsleer, P. & Dejonghe, H. 1994, A&A, 287, 43
Binney, J., Burnett, B., Kordopatis, G., et al. 2014, MNRAS, 439, 1231
Binney, J., Gerhard, O., & Spergel, D. 1997, MNRAS, 288, 365
Binney, J. & McMillan, P. 2011, MNRAS, 413, 1889
Binney, J. & Tremaine, S. 2008, Galactic Dynamics: Second Edition (Princeton University Press)
Bonaca, A., Hogg, D. W., Price-Whelan, A. M., & Conroy, C. 2018, arXiv e-prints [arXiv:1811.03631]
Bond, N. A., Ivezić, Ž., Sesar, B., et al. 2010, ApJ, 716, 1
Bovy, J. 2011, PhD thesis, New York University
Breddels, M. A. & Veljanoski, J. 2018, A&A, 618, A13
Büdenbender, A., van de Ven, G., & Watkins, L. L. 2015, MNRAS, 452, 956
Carrillo, I., Minchev, I., Kordopatis, G., et al. 2018, MNRAS, 475, 2679
Casetti-Dinescu, D. I., Girard, T. M., Korchagin, V. I., & van Altena, W. F. 2011, ApJ, 728, 7
Cui, X.-Q., Zhao, Y.-H., Chu, Y.-Q., et al. 2012, Research in Astronomy and Astrophysics, 12, 1197
de Zeeuw, T. 1985, MNRAS, 216, 273
Dehnen, W. 1998, AJ, 115, 2384
Dejonghe, H. & de Zeeuw, T. 1988, ApJ, 333, 90
Eggen, O. J. 1965, Moving Groups of Stars, ed. A. Blaauw & M. Schmidt (the University of Chicago Press), 111
Evans, N. W., Sanders, J. L., Williams, A. A., et al. 2016, MNRAS, 456, 4506
Famaey, B. & Dejonghe, H. 2003, MNRAS, 340, 752
Foreman-Mackey, D., Hogg, D. W., Lang, D., & Goodman, J. 2013, PASP, 125, 306
Gaia Collaboration, Brown, A. G. A., Vallenari, A., et al. 2018a, A&A, 616, A1
Gaia Collaboration, Brown, A. G. A., Vallenari, A., et al. 2016a, A&A, 595, A2
Gaia Collaboration, Katz, D., Antoja, T., et al. 2018b, A&A, 616, A11
Gaia Collaboration, Prusti, T., de Bruijne, J. H. J., et al. 2016b, A&A, 595, A1
Helmi, A., Babusiaux, C., Koppelman, H. H., et al. 2018, Nature, 563, 85
Hunt, J. A. S., Hong, J., Bovy, J., Kawata, D., & Grand, R. J. J. 2018, MNRAS, 481, 3794
Hunter, J. D. 2007, Computing in Science Engineering, 9, 90
Johnson, D. R. H. & Soderblom, D. R. 1987, AJ, 93, 864
King, III, C., Brown, W. R., Geller, M. J., & Kenyon, S. J. 2015, ApJ, 813, 89
Kluyver, T., Ragan-Kelley, B., Pérez, F., et al. 2016, in Positioning and Power in Academic Publishing: Players, Agents and Agendas, ed. F. Loizides & B. Scmidt (IOS Press), 87–90
Koppelman, H. H., Helmi, A., Massari, D., Roelenga, S., & Bastian, U. 2018, arXiv e-prints [arXiv:1812.00846]
Kunder, A., Kordopatis, G., Steinmetz, M., et al. 2017, AJ, 153, 75
Lindegren, L., Hernández, J., Bombrun, A., et al. 2018, A&A, 616, A2
Mackereth, J. T., Bovy, J., Leung, H. W., et al. 2019, arXiv e-prints [arXiv:1901.04502]
Majewski, S. R., Schiavon, R. P., Frinchaboy, P. M., et al. 2017, AJ, 154, 94
McMillan, P. J. 2011, MNRAS, 414, 2446
McMillan, P. J. 2017, MNRAS, 465, 76
Miyamoto, M. & Nagai, R. 1975, PASJ, 27, 533
Mood, A. M., Graybill, F. A., & Boes, D. C. 1974, Introduction to the Theory of Statistics: Third Edition (McGraw-Hill, Inc)
Navarro, J. F., Frenk, C. S., & White, S. D. M. 1996, ApJ, 462, 563
Oliphant, T. E. 2015, Guide to NumPy, 2nd edn. (USA: CreateSpace Independent Publishing Platform)
Piffl, T., Binney, J., McMillan, P. J., et al. 2014, MNRAS, 445, 3133
Poggio, E., Drimmel, R., Lattanzi, M. G., et al. 2018, MNRAS, 481, L21
Posti, L., Helmi, A., Veljanoski, J., & Breddels, M. A. 2018, A&A, 615, A70
Price-Whelan, A. M. & Bonaca, A. 2018, ApJ, 863, L20
Proctor, R. A. 1869, Proceedings of the Royal Society of London Series I, 18, 169
Quillen, A. C., Carrillo, I., Anders, F., et al. 2018, MNRAS, 480, 3132
Rao, C. R. 1973, Linear Statistical Inference and Its Applications: Second Edition (John Wiley & Sons, Inc.)
Reid, M. J., Menten, K. M., Brunthaler, A., et al. 2014, ApJ, 783, 130
Robin, A. C., Luri, X., Reylé, C., et al. 2012, A&A, 543, A100
Robin, A. C., Reylé, C., Derrière, S., & Picaud, S. 2003, A&A, 409, 523
Rose, C. & Smith, M. D. 2002, Mathematical Statistics with Mathematica (Springer-Verlag)
Schönrich, R. 2012, MNRAS, 427, 274
Schönrich, R., Binney, J., & Dehnen, W. 2010, MNRAS, 403, 1829
Sellwood, J. A., Trick, W. H., Carlberg, R. G., Coronado, J., & Rix, H.-W. 2019, MNRAS, 484, 3154
Siebert, A., Bienaymé, O., Binney, J., et al. 2008, MNRAS, 391, 793
Smith, M. C., Whiteoak, S. H., & Evans, N. W. 2012, ApJ, 746, 181
Smith, M. C., Wyn Evans, N., & An, J. H. 2009, ApJ, 698, 1110
Stuart, A. & Ord, J. K. 1987, Kendall's Advanced Theory of Statistics, Volume 1: Distribution Theory: Fifth Edition (Charles Griffin & Company Limited)
Taylor, M. B. 2005, in Astronomical Society of the Pacific Conference Series, Vol. 347, Astronomical Data Analysis Software and Systems XIV, ed. P. Shopbell, M. Britton, & R. Ebert, 29
Taylor, M. B. 2006, in Astronomical Society of the Pacific Conference Series, Vol. 351, Astronomical Data Analysis Software and Systems XV, ed. C. Gabriel, C. Arviset, D. Ponz, & S. Enrique, 666
Tian, H.-J., Liu, C., Wan, J.-C., et al. 2017, Research in Astronomy and Astrophysics, 17, 114
van de Ven, G., Hunter, C., Verolme, E. K., & de Zeeuw, P. T. 2003, MNRAS, 342, 1056
Veljanoski, J., Helmi, A., Breddels, M., & Posti, L. 2019, A&A, 621, A13
Wegg, C., Gerhard, O., & Bieth, M. 2018, ArXiv e-prints [arXiv:1806.09635]
Williams, M. E. K., Steinmetz, M., Binney, J., et al. 2013, MNRAS, 436, 101
Yanny, B., Rockosi, C., Newberg, H. J., et al. 2009, AJ, 137, 4377
York, D. G., Adelman, J., Anderson, Jr., J. E., et al. 2000, AJ, 120, 1579

Appendix A: Standard errors of sample (co)variances.

To estimate the error on the inferred tilt angles from *Method 1* of Sect. 3.2 we propagate the errors of the relevant velocity moments from Eq. 1.

The error on a sample variance, s^2, can be estimated (e.g. Rao 1973; Mood et al. 1974) by using

$$\mathrm{var}(s^2) = \frac{1}{N}\left(\mu_4 - \frac{N-3}{N-1}\mathrm{var}(v)^2\right) \tag{A.1}$$

for N stars. Here, μ_4 denotes the intrinsic 4$^{\mathrm{th}}$ central moment and $s^2 = \frac{1}{N-1}\sum_{i=1}^{N}(v_i - \langle v\rangle)^2$, for which v_i is the relevant velocity component, either v_R or v_z, of star i and $\langle v\rangle$ its mean taken over all stars in the bin considered. The intrinsic velocity moments are estimated by their observed values, which is a good approximation given the relatively small errors in the data for the bins explored.

The error on a sample covariance S_{xy} of x and y can be estimated (see Stuart & Ord (1987) or Rose & Smith (2002) for using mathStatica) by

$$\mathrm{var}(S_{xy}) = \frac{1}{N}\left[\mu_{22} - \frac{N-2}{N-1}\mathrm{cov}(x,y)^2 + \frac{1}{N-1}\mathrm{var}(x)\mathrm{var}(y)\right], \tag{A.2}$$

where $\mu_{22} = E[\{x - E(x)\}^2\{y - E(y)\}^2]$ for E denoting the expectation value. We have defined $S_{xy} = \frac{1}{N-1}\sum_{i=1}^{N}(x_i - \langle x\rangle)(y_i - \langle y\rangle)$. In our application x is replaced for v_R and y for v_z. The intrinsic moments are again estimated by taking the equivalent moments directly from the observed velocity distribution.

As an example for Sect. 3.2 we show in Fig. A.1 the error distributions for the bin at $R = 13.0$ and $z = 1.5$ kpc. This bin is near the edge of the volume investigated, but still contains 1772 stars. The vertical grey dashed lines indicate the values of the velocity moments that would be derived by using the data directly (i.e. not accounting for the errors). The medians of the error distributions are indicated by the vertical grey dotted lines. The recovered intrinsic velocity moments from *Method 1* are visualised by the vertical black solid lines (as here, these usually coincide with the vertical grey dashed lines). The dot-dashed lines show the recovered intrinsic velocity moment from *Method 2* which is very similar to that obtained with *Method 1*. Thus, even for this outer bin, the effects of measurement errors are relatively small.

Appendix B: The impact of a systematic parallax offset on the recovered tilt angles.

We here explain how a systematic parallax offset can effect the inferred tilt angles. For this purpose, we here only consider the (x,z)-plane and we assume that all parallaxes are shifted by the same offset $\Delta\varpi = -0.029$ mas.

For Galactic longitude l and latitude b the (U,V,W)-velocities in km/s can be computed the usual way (Johnson & Soderblom 1987; Bovy 2011):

$$\begin{pmatrix} U \\ V \\ W \end{pmatrix} = \begin{pmatrix} \cos(l)\cos(b) & -\sin(l) & -\cos(l)\sin(b) \\ \sin(l)\cos(b) & \cos(l) & -\sin(l)\sin(b) \\ \sin(b) & 0 & \cos(b) \end{pmatrix} \begin{pmatrix} v_{\mathrm{los}} \\ \frac{k}{\varpi}\mu_{l^\star} \\ \frac{k}{\varpi}\mu_b \end{pmatrix}. \tag{B.1}$$

Here, $\mu_{l^\star} = \mu_l\cos(b)$ and μ_b denote the proper motions in mas/yr in the direction of l and b, respectively, ϖ is the parallax in mas, and $k = 4.74047\frac{\mathrm{km/s}}{\mathrm{kpc\ mas/yr}}$ (assuming a Julian year).

When only considering an error in the parallaxes the "observed" velocities are affected as:

$$\begin{pmatrix} U \\ V \\ W \end{pmatrix}_1 = \begin{pmatrix} U \\ V \\ W \end{pmatrix}_0 + \frac{\partial}{\partial\varpi}\begin{pmatrix} U \\ V \\ W \end{pmatrix}\Bigg|_0 \Delta\varpi + O(\Delta\varpi^2). \tag{B.2}$$

Subscript 0 denotes the true position and velocities, subscript 1 the "observed" quantities. Furthermore:

$$\frac{\partial}{\partial\varpi}\begin{pmatrix} U \\ V \\ W \end{pmatrix} = -\frac{1}{\varpi}\begin{pmatrix} U - \cos(l)\cos(b)\, v_{\mathrm{los}} \\ V - \sin(l)\cos(b)\, v_{\mathrm{los}} \\ W - \sin(b)\, v_{\mathrm{los}} \end{pmatrix}, \tag{B.3}$$

and:

$$v_{\mathrm{los}} = \cos(b)\cos(l)\, U + \cos(b)\sin(l)\, V + \sin(b)\, W. \tag{B.4}$$

Let us now define the tilt angle δ as:

$$\tan(2\delta) = \frac{2\mathrm{cov}(U,W)}{\mathrm{var}(U) - \mathrm{var}(W)}. \tag{B.5}$$

In a steady state axisymmetric system $\langle v_R\rangle = \langle v_z\rangle = 0$. Therefore, at the (x,z)-plane $\langle U\rangle = \langle W\rangle = 0$, and thus $\mathrm{var}(U) = \langle U^2\rangle$, $\mathrm{var}(W) = \langle W^2\rangle$, and $\mathrm{cov}(U,W) = \langle UW\rangle$. For $l = 0°$ and $l = 180°$ we also notice that $U = -v_R$ and $W = v_z$, and therefore that $\delta = -\gamma$. In the remainder of this Appendix we refer to δ when we use 'tilt angle' (unless stated otherwise).

Plugging Eq. B.2 up to first order in $\frac{\Delta\varpi}{\varpi_0}$ into Eq. B.5 we get:

$$\tan(2\delta_1) \simeq \frac{2\langle U_0W_0\rangle + \epsilon_{\mathrm{A}}}{\langle U_0^2\rangle - \langle W_0^2\rangle + \epsilon_{\mathrm{B}}}, \tag{B.6}$$

in which:

$$\begin{aligned} \epsilon_A &= \left[\pm\left(\langle U_0^2\rangle + \langle W_0^2\rangle\right)\sin(2b) - 2\langle U_0W_0\rangle\right]\left(\frac{\Delta\varpi}{\varpi_0}\right) \\ \epsilon_B &= 2\left[\langle W_0^2\rangle\cos^2(b) - \langle U_0^2\rangle\sin^2(b)\right]\left(\frac{\Delta\varpi}{\varpi_0}\right), \end{aligned} \tag{B.7}$$

where $\pm$ holds for $l \in \left\{\begin{matrix} 0° \\ 180° \end{matrix}\right\}$.

To further explore the effect of a shift in the parallaxes we now investigate what would happen to the tilt angles in two different cases of alignment: spherical alignment and cylindrical alignment.

We start by rewriting Eq. B.6 into the form of

$$\begin{aligned} \delta_1 &= \frac{1}{2}\arctan\left[(1+x)\tan(2\delta_0)\right] \\ \delta_1 &= \delta_0 + \frac{1}{4}\sin(4\delta_0)\, x + O(x^2) \\ \Delta\delta &\simeq \frac{1}{4}\sin(4\delta_0)\, x. \end{aligned} \tag{B.8}$$

We then get:

$$\begin{aligned} \tan(2\delta_1) &\simeq \frac{2\langle U_0W_0\rangle}{\langle U_0^2\rangle - \langle W_0^2\rangle}\left[\frac{1-\epsilon_{\mathrm{C}}}{1-\epsilon_{\mathrm{D}}}\right] \\ \tan(2\delta_1) &\simeq \tan(2\delta_0)\left[\frac{1-\epsilon_{\mathrm{C}}}{1-\epsilon_{\mathrm{D}}}\right], \end{aligned} \tag{B.9}$$

in which:

$$\begin{aligned} \epsilon_{\mathrm{C}} &= \left[1 \mp \left(\frac{\langle U_0^2\rangle + \langle W_0^2\rangle}{2\langle U_0W_0\rangle}\right)\sin(2b)\right]\left(\frac{\Delta\varpi}{\varpi_0}\right) \\ \epsilon_{\mathrm{D}} &= 2\left[\frac{\langle U_0^2\rangle\sin^2(b) - \langle W_0^2\rangle\cos^2(b)}{\langle U_0^2\rangle - \langle W_0^2\rangle}\right]\left(\frac{\Delta\varpi}{\varpi_0}\right). \end{aligned} \tag{B.10}$$

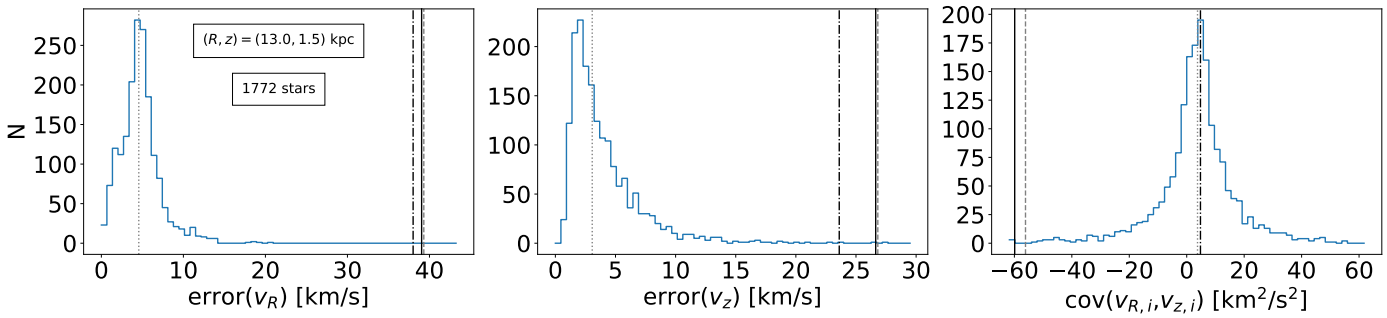

Fig. A.1. Error distributions for the bin at $R = 13.0$ and $z = 1.5$ kpc for the different velocity components: v_R (left), v_z (middle), and its covariance (right). The corresponding medians of the error distributions are shown by the vertical grey dotted lines. The vertical grey dashed lines indicate the values of the velocity moments taken from the data directly (i.e. not accounting for the errors). The black vertical solid lines and dot-dashed lines show the recovered intrinsic velocity moment from *Method 1* and *Method 2* respectively (see Sect. 3). Even at this bin, which still contains 1772 stars, the impact of the measurement errors on the recovered velocity moments is relatively small.

Then under the assumptions that $|\epsilon_C| \ll 1$ and $|\epsilon_D| \ll 1$ we get:

$$x \simeq \epsilon_{\rm D} - \epsilon_{\rm C} \,. \tag{B.11}$$

We highlight the effects for four different latitudes:

$$\begin{aligned}
b = 0^\circ : \qquad & x = -\left(\frac{\Delta\varpi}{\varpi_0}\right)\left[\frac{\langle U_0^2\rangle + \langle W_0^2\rangle}{\langle U_0^2\rangle - \langle W_0^2\rangle}\right] \\
|b| = 90^\circ : \qquad & x = +\left(\frac{\Delta\varpi}{\varpi_0}\right)\left[\frac{\langle U_0^2\rangle + \langle W_0^2\rangle}{\langle U_0^2\rangle - \langle W_0^2\rangle}\right] \\
b = +45^\circ : \qquad & x = \pm\left(\frac{\Delta\varpi}{\varpi_0}\right)\left[\frac{\langle U_0^2\rangle + \langle W_0^2\rangle}{2\langle U_0 W_0\rangle}\right] \\
b = -45^\circ : \qquad & x = \mp\left(\frac{\Delta\varpi}{\varpi_0}\right)\left[\frac{\langle U_0^2\rangle + \langle W_0^2\rangle}{2\langle U_0 W_0\rangle}\right] .
\end{aligned} \tag{B.12}$$

Since the velocity ellipse is mostly non-tilted ($\delta_0 = 0^\circ$) at the Galactic midplane the inferred tilt angles at $b = 0^\circ$ are not affected by an error in the parallax. Geometrically this is not surprising since, at $b = 0^\circ$, the U-component of the velocities are not affected. The W-velocities are only inflated and will not change the tilt angle. However, if $\delta_0 \neq 0^\circ$, then, since for typical values of the velocity moments at the midplane $\sigma(v_R) > \sigma(v_z)$ (see e.g. Gaia Collaboration et al. 2018b), the term between the square brackets is larger than one. The inferred tilt angle will therefore be steeper (more positive if $\delta_0 > 0^\circ$ and more negative if $\delta_0 < 0^\circ$). At $|b| = 90^\circ$ the effect is reversed and the tilt angles will become shallower (less positive if $\delta_0 > 0^\circ$ and less negative if $\delta_0 < 0^\circ$) due to the parallax offset. For the case of spherical alignment the relation $\tan(2\delta_0) = \tan(2\theta)$ can be applied.

The approximations used so far fail for $\langle U_0 W_0\rangle \simeq 0$, since then $|\epsilon_{\rm C}| \not\ll 1$, and for $\langle U_0^2\rangle \simeq \langle W_0^2\rangle$, since then $|\epsilon_{\rm D}| \not\ll 1$, and thus $|x| \not\ll 1$. In the case of cylindrical alignment ($\delta_0 = \langle U_0 W_0\rangle = 0$) and for $|\epsilon_{\rm D}| \ll 1$ we get[2]:

$$\delta_1 \simeq \pm\frac{1}{2}\sin(2b)\left(\frac{\langle U_0^2\rangle + \langle W_0^2\rangle}{\langle U_0^2\rangle - \langle W_0^2\rangle}\right)\left(\frac{\Delta\varpi}{\varpi_0}\right) , \tag{B.13}$$

where we used that $\tan(2\delta_1) \simeq 2\delta_1$ for small deviations around $\delta_1 = 0^\circ$. This means that at $l = 0$ ($l = 180^\circ$) and for $\sigma(v_R) > \sigma(v_z)$ the tilt angles appear to be negative (positive) for $b > 0^\circ$, and positive (negative) for $b < 0^\circ$.

[2] If, hypothetically, both $\langle U_0^2\rangle = \langle W_0^2\rangle$ and $\langle U_0 W_0\rangle = 0$, then $\tan(2\delta_1) = \pm\tan(2b)$.

We have inserted the relevant Galactic velocity dispersions as a function of R and z and set the covariance term such that there is either spherical or cylindrical alignment throughout the extent of the dataset. We find that the tilt angles are affected very similarly. This is visualised in Fig. B.1 (recall that $\gamma = -\delta$ since we here consider $l = 0^\circ$ and $l = 180^\circ$ only). We therefore think that our test performed in Sect. 5.1 is realistic, even though the intrinsic tilt angles of the GUMS catalogue are more or less cylindrically aligned.

Besides the fact that the orientation of the velocity ellipse changes due to the parallax offset, obviously the stars under consideration also move in position. Thus, in fact a sample of stars with tilt angle δ_0 at parallax ϖ_0 gets "observed" at ϖ_1 with tilt angle δ_1. We have not taken this effect into account in the analytic description from this Appendix.

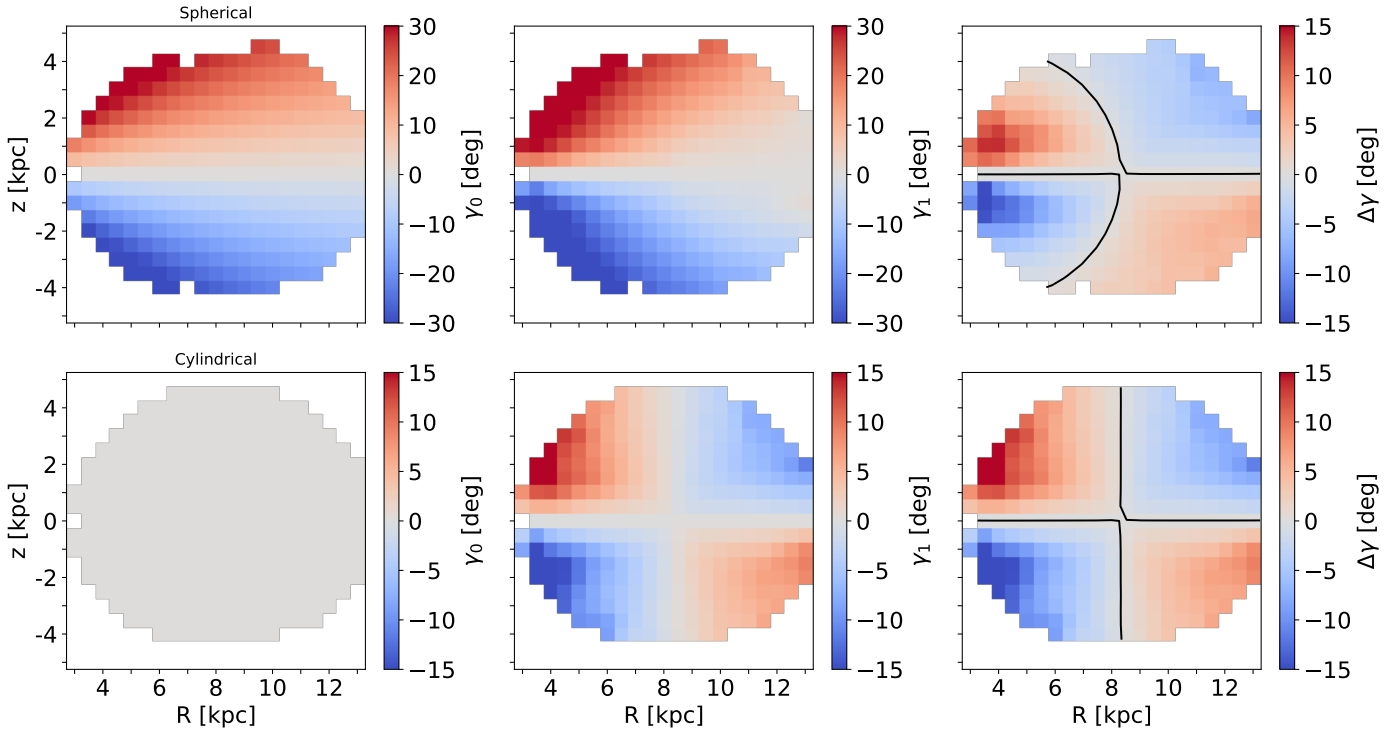

Fig. B.1. The effect of a constant shift in the parallaxes of the stars ($\Delta\varpi = -0.029$ mas) on the tilt angle γ, as measured in galactocentric cylindrical coordinates for different types of intrinsic alignment. The left columns show intrinsic tilt angles γ_0 as a function of R and z. The middle columns show the tilt angles γ_1 computed from the "observed" velocity moments. The right column shows $\Delta\gamma = \gamma_1 - \gamma_0$. Be aware of the different colorbar ranges. In the top panels we set the velocity covariances such that the input alignment is spherical. In the bottom panels the input alignment is cylindrical. Black contours denote regions where the tilt angle is not affected, i.e. $\Delta\gamma = 0°$. For spherical alignment this is expected to be the case at $z \approx z_\odot \approx 0$ kpc and on the circle that goes through the Galactic centre and $R = R_\odot$. For cylindrical alignment this is expected to occur at both $z = 0$ kpc and $R = R_\odot$.